Vietnam Journal of Mechanics, Vietnam Academy of Science and Technology
DOI: https://doi.org/10.15625/0866-7136/22420

INTEGRATING REACTION-DIFFUSION EQUATIONS WITH A DYNAMIC BODY-FITTED TRIMMED MESH TECHNIQUE FOR LEVEL SET-BASED STRUCTURAL OPTIMIZATION

Ba-Dinh Nguyen-Tran[1], **Son H. Nguyen**[2,3], **Duc-Huynh Phan**[1,*], **Quoc Hoa Pham**[4], **Trung Nguyen-Thoi**[3,5]

[1]*Faculty of Civil Engineering, Ho Chi Minh City University of Technology and Education, Vietnam*
[2]*Laboratory for Computational Mechanics, Institute for Computational Science and Artificial Intelligence, Van Lang University, Ho Chi Minh City, Vietnam*
[3]*Faculty of Mechanical, Electrical, and Computer Engineering, Van Lang School of Technology, Van Lang University, Ho Chi Minh City, Vietnam*
[4]*Faculty of Basic Engineering, Tran Dai Nghia University, Ho Chi Minh City, Vietnam*
[5]*Laboratory for Applied and Industrial Mathematics, Institute for Computational Science and Artificial Intelligence, Van Lang University, Ho Chi Minh City, Vietnam*
[*]E-mail: huynhpd@hcmute.edu.vn

Received: 16 February 2025 / Revised: 10 November 2025 / Accepted: 14 November 2025
Published online: 05 December 2025

Abstract. In this study, a dynamic body-fitted trimmed mesh approach is presented to address reaction-diffusion equation-based topology optimization problems, with the objective of minimizing structural compliance. The evolution of the zero-isoline of a level set function is governed by the solution of a reaction-diffusion equation, which is controlled by the topological sensitivity field and implemented on a regular background quadrilateral mesh. During each optimization iteration, a dynamic body-fitted trimmed mesh is constructed to accurately delineate the structural domain. This procedure employs the marching square algorithm, which segments the fixed background quadrilateral mesh along the zero-isoline of the level set function. To ensure precision in the optimization, the reaction-diffusion equation is solved utilizing a numerical algorithm grounded in the exact volume constraint method, which meticulously calculates the Lagrange multiplier to uphold the constraint condition. The proposed approach exhibits exceptional efficacy in solving level set-based topology optimization challenges, particularly in achieving accurate boundary representations while strictly adhering to volume constraint conditions within a predefined error tolerance. These are evident through the numerical results of two benchmark problems including 2D cantilever beam and L-bracket domain.

Keywords: body-fitted trimmed mesh, level set function, reaction-diffusion equation, marching square algorithm, exact volume constraint method.

1. INTRODUCTION

In the field of topology optimization (TO), the level set (LS) method is widely recognized for its versatility in engineering design. Its innovative use of scalar functions in higher-dimensional spaces to implicitly define material boundaries has made it a key tool for creating lightweight, high-performance structures that meet specific criteria [1]. Typically, the evolution of the LS function is governed by solving the Hamilton-Jacobi equation, in which shape sensitivity is considered as a normal velocity field along the free boundary during the optimization process. Solving this equation requires implementing a re-initialization procedure for the LS function after certain iterations to preserve its signed distance function (SDF) property. This procedure is both computationally intensive and challenging. Additionally, this approach has one notable weakness in that it is impossible to create new holes in the material region, which requires laying a sufficient number of holes in the initial design configuration to avoid the local convergence phenomenon [2]. To address these issues, a few variational formulations replacing the Hamilton-Jacobi equation have been developed in the literature such as the radial basis [2, 3] and reaction-diffusion equations [4, 5]. Among these two variational formulations, the reaction-diffusion equation (RDE) presents a more straightforward mathematical model and has been widely used in LS-based TO. This methodology not only enables topological alterations that generate new boundaries during the optimization process without necessitating the re-initialization of the LS function, but it also offers a mechanism for qualitative control over the geometric complexity of the optimized configurations. This control is achieved through the careful selection of appropriate values for the regularization parameter within the diffusion component.

Most conventional LS-based topology optimization (TO) methods convert the LS function into a density distribution, commonly referred to as the "Ersatz material" [6], and utilize a fixed Eulerian mesh to solve the state equations. However, this approach can lead to the zig-zag boundary phenomenon in the finite element (FE) analysis, similar to issues observed in density-based TO methods [7,8]. This phenomenon can significantly influence the final optimal shapes. To address these challenges, various research efforts have introduced conforming discretization methods, such as body-fitted mesh evolution techniques [1], boundary element methods (BEM) [9], and anisotropic mesh adaptation approaches [10]. These methods offer the advantage of providing a clear and explicit representation of the structural (material) domain in LS-based TO. However, they demand the implementation of efficient meshing techniques. Despite advancements, the prevalent use of triangular/tetrahedral meshes in prior studies has been associated with issues such as low computational efficiency and increased costs in efforts to improve mesh quality.

Recently, Nguyen et al. [11, 12] introduced a new dynamic body-fitted mesh evolution method utilizing trimmed hexahedral meshes for the optimization of 3D problems based on the LS framework. This approach was subsequently extended to optimize plate and shell structures by employing trimmed quadrilateral (Q4) elements [13]. Trimmed Q4 elements are efficiently generated using the marching square (MS) algorithm [14], which splits regular background Q4 elements into polygonal ones along the zero-isoline of an LS function, as illustrated in Fig. 1. These elements are recognized for their considerable versatility, accommodating an arbitrary number of vertices and edges while maintaining high accuracy. Additionally, removing the void domain from the FE analysis during the optimization process can substantially decrease computational expenses.

In numerous previous studies, the augmented Lagrangian (AL) method and its variations have been widely employed to address LS-based TO problems. However, applying this method for the volume-based TO problems has a noticeable drawback in not guaranteeing the accuracy of the volume constraint in the final optimization configuration [15]. To address this limitation, several studies have been proposed in the literature. For instance, Cui et al. (2022) [3] presented a fuzzy PID control algorithm to compute the value of the Lagrange multiplier as well as address the volume constraint. While this method demonstrates excellent numerical stability and high accuracy in maintaining the volume constraint for optimal designs, its application to TO problems is hindered by the complexity of mathematical modeling and the challenge of selecting appropriate initial PID control parameters. In another approach, Cui et al. (2023) [15] introduced an exact volume constraint method (EVCM) for TO via the RDE based on accurately computing the value of the Lagrange multiplier. Their approach separates the LS function and the RDEs into two independent components associated with the Lagrange multiplier. During each optimization iteration, two distinct LS functions are computed, followed by the application of an interior Newton-Raphson algorithm to accurately determine the Lagrange multiplier. This ensures that the volume constraint is tightly satisfied at each step. Numerical examples demonstrated that this method significantly enhances numerical stability and improves convergence efficiency in TO problems.

Building on these insights, this paper presents a novel integration of RDE with the dynamic body-fitted trimmed Q4 mesh technique, aimed at establishing an efficient and robust framework for solving structural optimization problems. Notably, the void domain will be removed from the FE analysis during the optimization process to reduce computational expenses and mitigate the occurrence of singularity phenomena.

2. DYNAMIC BODY-FITTED TRIMMED MESH PROCEDURE FOR SOLVING LS-BASED TOPOLOGY OPTIMIZATION

2.1. Dynamic body-fitted trimmed Q4 mesh technique

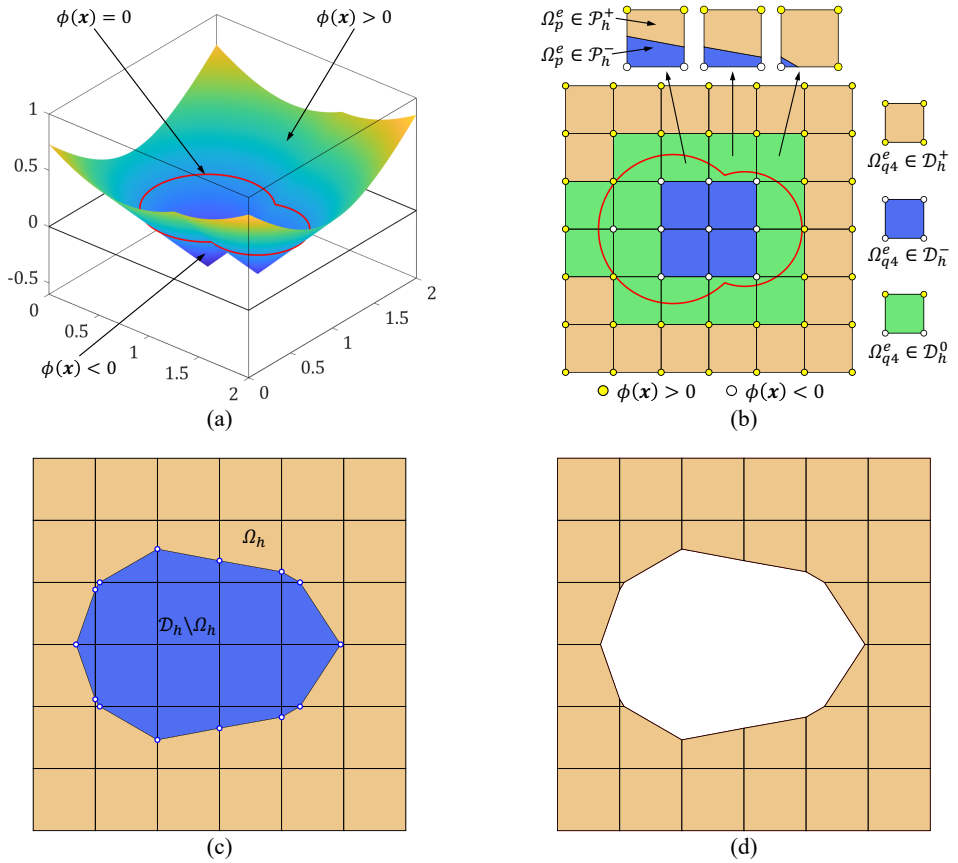

Fig. 1. Dynamic body-fitted mesh evolution method: (a) surface representation, (b) three non-overlapping subdomains and element-trimmed method for $\mathcal{D}_h^0$ subdomain, (c) body-fitted trimmed Q4 mesh, and (d) body-fitted trimmed Q4 mesh with only material domain

We define $\mathcal{D} \subset \mathbb{R}^2$ as a fixed design domain accommodating an open bounded material domain $\Omega \subset \mathcal{D}$ which involves all admissible shapes of TO problems. The boundary of Ω is $\partial\Omega := \Gamma = \Gamma_D \cup \Gamma_N \cup \Gamma_0$ such that $\Gamma_D \cap \Gamma_N = \varnothing$, where Γ_D and Γ_N are the Dirichlet and Neumann boundaries, respectively, and Γ_0 is the design boundary whose shape changes throughout the optimization process. As introduced by Yamada et al. (2010) [4], Fig. 1(a) reveals a modified LS function $\phi(\boldsymbol{x})$: $\mathcal{D} \rightarrow \mathbb{R}$, derived from the phase field model, is utilized to delineate the material domain $\Omega \backslash \partial\Omega$, its boundary $\partial\Omega$, and the void

domain $\mathcal{D}\backslash\Omega$, as described by the following definition

$$\begin{cases} 1 \geq \phi(\boldsymbol{x}) > 0, & \forall \boldsymbol{x} \in \Omega\backslash\partial\Omega \\ \phi(\boldsymbol{x}) = 0, & \forall \boldsymbol{x} \in \partial\Omega \\ 0 > \phi(\boldsymbol{x}) \geq -1, & \forall \boldsymbol{x} \in \mathcal{D}\backslash\Omega \end{cases} \tag{1}$$

where in regions sufficiently far from the material boundaries, the level set function consistently takes on values of 1 or -1. Assume that the domain $\mathcal{D}$ is discretized into a uniform regular Q4 mesh $\mathcal{D}_h$ such that $\mathcal{D}_h = \bigcup_{e=1}^{n_\gamma} \Omega_{Q4}^e$ and $\Omega_{Q4}^i \cap \Omega_{Q4}^j = \varnothing$ for $i \neq j$, wherein n_e is the number of elements. Based on the information regarding the zero-isoline, three distinct and non-overlapping subdomains $\mathcal{D}_h^0$, $\mathcal{D}_h^+$, and $\mathcal{D}_h^-$ are partitioned from the domain $\mathcal{D}_h$, as illustrated in Fig. 1(b), such that

$$\mathcal{D}_h = \mathcal{D}_h^+ \cup \mathcal{D}_h^- \cup \mathcal{D}_h^0 \quad \text{with} \quad \begin{cases} \mathcal{D}_h^- = \left\{ \Omega_{Q4}^e \in \mathcal{D}_h \,|0 > \forall\phi(\boldsymbol{x}) \geq -1 \right\}, \\ \mathcal{D}_h^+ = \left\{ \Omega_{Q4}^e \in \mathcal{D}_h \,|1 \geq \forall\phi(\boldsymbol{x}) > 0 \right\}, \\ \mathcal{D}_h^0 = \left\{ \Omega_{Q4}^e \in \mathcal{D}_h \,\middle|\, \Omega_{Q4}^e \cap \Gamma \neq 0 \right\}, \end{cases} \tag{2}$$

As shown in Fig. 1(b), the $\mathcal{D}_h^0$ subdomain is distinctly organized into polygonal element domains, denoted as $\mathcal{P}_h^+ = \left\{ \Omega_p^e \in \mathcal{D}_h^0 \,|1 \geq \forall\phi(\boldsymbol{x}) > 0 \right\}$ and $\mathcal{P}_h^- = \left\{ \Omega_p^e \in \mathcal{D}_h^0 \,|0 > \forall\phi(\boldsymbol{x}) \geq -1 \right\}$ containing the polygonal elements constructed based on the MS algorithm [14]. Therein, a point $\boldsymbol{x}_I$ (i.e. $\phi(\boldsymbol{x}_I) = 0$) is the intersection between an LS function and an edge of a Q4 element defined by linear interpolation as follows

$$\boldsymbol{x}_I = \boldsymbol{x}_1 - \frac{\phi(\boldsymbol{x}_1)}{\phi(\boldsymbol{x}_1) - \phi(\boldsymbol{x}_2)} (\boldsymbol{x}_1 - \boldsymbol{x}_2), \tag{3}$$

where $\boldsymbol{x}_1$ and $\boldsymbol{x}_2$ denote the positions of the endpoints on an edge of a Q4 element, ensuring that their LS values satisfy the condition $\phi(\boldsymbol{x}_1) \cdot \phi(\boldsymbol{x}_2) < 0$. Leveraging the reflective and rotational symmetry in the analyzed configurations, the number of intersection topologies in this algorithm can be reduced from 16 to 4, as depicted in Fig. 2. After

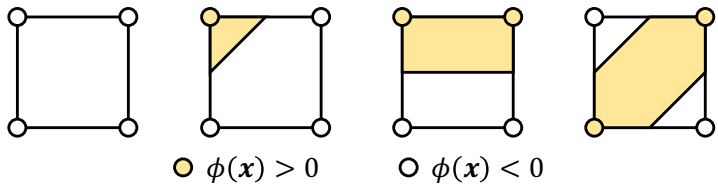

Fig. 2. Four MS configurations for a regular Q4 element trimmed by a zero-isoline of an LS function

partitioning $\mathcal{D}_h^0$, the two trimmed subdomains merge with $\mathcal{D}_h^+$ and $\mathcal{D}_h^-$ to form the material and void domains, Ω_h and $\mathcal{D}_h \backslash \Omega_h$, respectively. This results in $\Omega_h = \mathcal{D}_h^+ \cup \mathcal{P}_h^+$ and $\mathcal{D}_h \backslash \Omega_h = \mathcal{D}_h^- \cup \mathcal{P}_h^-$, as illustrated in Fig. 1(c).

Next, a handling procedure to enhance the quality of trimmed Q4 elements at material boundaries is implemented by merging the adjacent nodes of polygonal elements with small edges within a specified tolerance into one node, as illustrated in Fig. 3. Lastly, the well-known Wachspress coordinates, recognized for their simplicity in generating interpolation functions for the FE framework, is applied in this study. Comprehensive details regarding these polygonal shape functions can be found in [16]. Additionally, in this study, the void domain will be removed from the FE analysis during the optimization process to reduce computational expenses and mitigate the occurrence of singularity phenomena, as shown in Fig. 1(d).

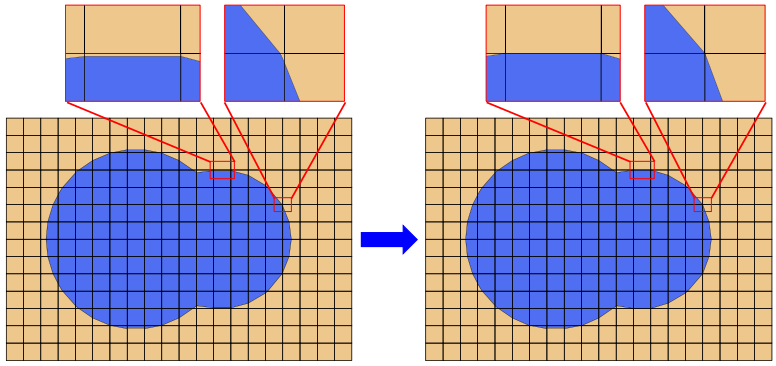

Fig. 3. Progress to improve the quality of trimmed Q4 at the material boundary

2.2. Level set-based topology optimization using reaction-diffusion-based approach

Using a dynamic body-fitted trimmed mesh approach for the LS-based TO, a general minimum compliance problem formulated under a volume constraint G is expressed as follows

$$\begin{cases} \text{Find } \phi = \phi\left(\boldsymbol{X}\right), \quad \forall \boldsymbol{X} \in \mathcal{D}, \\ \inf\limits_{\phi} \Psi\left(\boldsymbol{u}\right) = \displaystyle\int_{\Omega} \boldsymbol{\varepsilon}^T\left(\boldsymbol{u}\right) \mathfrak{C} \boldsymbol{\varepsilon}\left(\boldsymbol{u}\right) \mathrm{d}\Omega, \\ \text{s.t.} \begin{cases} a\left(\boldsymbol{u}, \boldsymbol{v}\right) = l\left(\boldsymbol{v}\right), \\ G\left(\phi\right) = \displaystyle\int_{\mathcal{D}} \chi_{\phi}\left(\phi\right) \mathrm{d}\mathcal{D} - V_{\lim} \leq 0, \end{cases} \\ \boldsymbol{u} \in \mathbb{U}, \boldsymbol{v} \in \mathbb{V}, \end{cases} \quad \text{with} \quad \begin{cases} a\left(\boldsymbol{u}, \boldsymbol{v}\right) = \displaystyle\int_{\Omega} \boldsymbol{\varepsilon}^T\left(\boldsymbol{u}\right) \mathfrak{C} \boldsymbol{\varepsilon}\left(\boldsymbol{v}\right) \mathrm{d}\Omega, \\ l\left(\boldsymbol{v}\right) = \displaystyle\int_{\Gamma} \boldsymbol{f}^T \boldsymbol{v} \mathrm{d}\Gamma, \end{cases} \tag{4}$$

where $\boldsymbol{u}\left(\boldsymbol{x}\right)$ and $\boldsymbol{v}\left(\boldsymbol{x}\right)$ are the displacement and virtual displacement vectors of the material domain, respectively; $\mathfrak{C}$ is the constant material matrix; $\boldsymbol{f}\left(\boldsymbol{x}\right)$ is the load vector; $\Psi\left(\boldsymbol{u}\right)$

is the general objective function; $\boldsymbol{\varepsilon}(\boldsymbol{u}) = \frac{1}{2}\left(\nabla \boldsymbol{u} + (\nabla \boldsymbol{u})^T\right)$ is the strain vector; V_{lim} is the volume limit; $\mathbb{U} \in \mathbb{H}^1(\Omega)$ and $\mathbb{V} \in \mathbb{H}^1(\Omega)$ are the FE approximation spaces; and $\chi_\phi(\phi)$ is the characteristic function which will be discussed in Section 2.4. Note that $\boldsymbol{X}$ and $\boldsymbol{x}$ denote the positions in the regular Q4 mesh of the fixed design domain and the body-fitted trimmed mesh of the material domain, respectively.

By using the Lagrange multiplier method [5], the optimization problem (4) is replaced by the unconstrained one,

$$\mathfrak{L}(\boldsymbol{u}, v, \phi, \lambda) = \Psi(\boldsymbol{u}) + a(\boldsymbol{u}, v) - l(v) + \lambda G(\phi), \tag{5}$$

where $\mathfrak{L}$ and λ are the augmented Lagrangian functional and the Lagrange multiplier, respectively. During the optimization process, an optimal configuration is determined if it satisfies the following KKT (Karush-Kuhn-Tucker) conditions [5]:

$$\mathfrak{L}' = 0, \quad \lambda G = 0, \quad \lambda \geq 0, \quad G \leq 0, \tag{6}$$

where $\mathfrak{L}'$ denotes the derivative of $\mathfrak{L}$. Initially, the formulation of $\mathfrak{L}'$ in the LS-based TO problem is predominantly conducted using the classical method, which relies on shape sensitivity analysis [6]. However, this approach has a critical limitation: it cannot generate new holes within the material region. As a result, the initial design configuration must include a sufficiently large number of holes to mitigate the risk of local convergence, which can adversely affect the solution quality [2]. To overcome this limitation, Yamada et al. (2010) [4] introduced the use of topological sensitivity to define $\mathfrak{L}'$. Subsequently, Otomori et al. (2015) [5] further developed it by considering the effect of the boundary condition of the holes when new holes were created in the material domain during the optimization process. Due to the self-adjoint nature of the minimum compliance problem, the topological derivative of the Lagrangian $\mathfrak{L}$ on the material domain is expressed as follows

$$d_t \mathfrak{L}(\boldsymbol{x})|_\Omega = \lambda - \underbrace{\boldsymbol{\varepsilon}_0^T \boldsymbol{A} \boldsymbol{\varepsilon}_0}_{\mathcal{J}(\boldsymbol{x})}, \tag{7}$$

where $\mathcal{J}(\boldsymbol{x})$ is the strain energy density and the subscript "0" denotes the values obtained without creating holes. In Eq. (7), $\boldsymbol{A}$ is a material matrix given in [5].

Based on the *extended* topological derivative (discussed in Section 2.3) of the Lagrangian $\mathfrak{L}$ on the fixed design domain [4, 5], the LS function ϕ is updated during the optimization process by solving the RDE with a fictitious time t as follows

$$(\mathcal{E}_0): \begin{cases} \dfrac{\partial \phi}{\partial t} = -\mathfrak{K}\left(-\zeta \cdot d_t \mathfrak{L}(\boldsymbol{X})|_{\mathcal{D}} - \tau \nabla^2 \phi\right), & \text{in } \mathcal{D} \\ \dfrac{\partial \phi}{\partial n} = 0, & \text{on } \partial\mathcal{D} \backslash \partial\mathcal{D}_N \\ \phi = 1, & \text{on } \partial\mathcal{D}_N \end{cases} \tag{8}$$

where $\Re(\phi)$ is a coefficient of proportionality set to be 1; $\tau\nabla^2\phi$ is the regularization diffusion term which ensures the smoothness of the LS function; τ is a regularization parameter; $\zeta = \dfrac{\int_{\mathcal{D}} \mathrm{d}\mathcal{D}}{\int_{\mathcal{D}} |\mathcal{J}(\boldsymbol{X})| \, \mathrm{d}\mathcal{D}}$ is an extended parameter designed for sensitivity normalization [5]; and $\partial\mathcal{D} = \partial\mathcal{D}_N \cup \partial\mathcal{D}_D$ is the boundary of $\mathcal{D}$, in which $\partial\mathcal{D}_N$ and $\partial\mathcal{D}_D$ are respectively the Neumann and Dirichlet boundary conditions of the design domain $\mathcal{D}$.

2.3. Extension and smoothing of the topological sensitivity field

In the LS-based TO framework using a body-fitted trimmed mesh approach, the topological derivative of the Lagrangian in Eq. (7) is only meaningful within the material domain Ω_h. However, to solve the RDE, the topological derivative governing the evolution of the LS function must be defined across the entire fixed design domain $\mathcal{D}_h$ [11]. To achieve this, our approach extends the topological derivative field from the material domain, $d_t\mathfrak{L}(\boldsymbol{x})|_{\Omega}$, to the entire fixed design domain, $d_t\mathfrak{L}(\boldsymbol{X})|_{\mathcal{D}}$, as follows

$$d_t\mathfrak{L}(\boldsymbol{X})|_{\mathcal{D}} = \begin{cases} \lambda - \mathcal{J}(\boldsymbol{X}), & \forall \boldsymbol{X} \in \Omega_h \\ \lambda, & \forall \boldsymbol{X} \in \mathcal{D}_h \backslash \Omega_h \end{cases} \tag{9}$$

where $\mathcal{J}(\boldsymbol{X})$ is the strain energy density extended to the fixed design domain $\mathcal{D}_h$. Note that this strain energy density is not continuous across the zero-isoline Γ_0 of the LS function (intermediate domain) [11]. To mitigate this discontinuity, several techniques have been introduced in previous research such as the fast extension method [17], fast local level set method [18], and simple radial smoothing filter [11]. Among these methods, the simple radial smoothing filter is one of the simple techniques that achieves the smoothness of the strain energy density field. Hence, in this paper, a strain energy density in the intermediate domain $\mathcal{D}_h^0$ is smoothed using the simple radial smoothing filter [11], defined as

$$\hat{\mathcal{J}}(\boldsymbol{X}) = \begin{cases} \dfrac{\sum_{\boldsymbol{X}_r \in n_r} \Phi_r(\|\boldsymbol{X}_r - \boldsymbol{X}\|_2) \cdot \mathcal{J}(\boldsymbol{X})}{\sum_{\boldsymbol{X}_r \in n_r} \Phi_r(\|\boldsymbol{X}_r - \boldsymbol{X}\|_2)}, & \forall \boldsymbol{X} \in \mathcal{D}_h^0 \\ \mathcal{J}(\boldsymbol{X}), & \forall \boldsymbol{X} \in \mathcal{D}_h \backslash \mathcal{D}_h^0 \end{cases} \tag{10}$$

where

$$\Phi_r(\|\boldsymbol{X}_r - \boldsymbol{X}\|_2) = \max(0, r_{\min} - \|\boldsymbol{X}_r - \boldsymbol{X}\|_2), \tag{11}$$

is a weight function, n_r denotes the set of grid points $\boldsymbol{X}_r$ for which the distance $\|\boldsymbol{X}_r - \boldsymbol{X}\|_2$ is smaller than the filter radius $r_{\min}$. Finally, the topological derivative field across the entire design domain can be redefined as

$$d_t\mathfrak{L}(\boldsymbol{X})|_{\mathcal{D}} = \begin{cases} \lambda - \mathcal{J}(\boldsymbol{X}), & \forall \boldsymbol{X} \in \mathcal{D}_h^+ \\ \lambda, & \forall \boldsymbol{X} \in \mathcal{D}_h^- \\ \lambda - \hat{\mathcal{J}}(\boldsymbol{X}), & \forall \boldsymbol{X} \in \mathcal{D}_h^0 \end{cases} \tag{12}$$

where subdomains $\mathcal{D}_h^0$, $\mathcal{D}_h^+$, and $\mathcal{D}_h^-$ are defined in Section 2.1.

2.4. Exact volume constraint method

To determine the value of the Lagrange multiplier λ in Eq. (12), Otomori et al. (2015) [5] introduced a modified version of the augmented Lagrangian (AL) method as follows

$$\lambda = \left(\frac{\int_{\mathcal{D}} \hat{\mathcal{J}}\left(\boldsymbol{X}\right) \mathrm{d}\mathcal{D}}{\int_{\mathcal{D}} \mathrm{d}\mathcal{D}} \exp\left[\alpha_1 \left(\frac{G}{G_{\mathrm{lim}}} + \alpha_2 \right)\right] \right), \tag{13}$$

with the volume constraint G in Eq. (4) is replaced with the following form

$$G = \int_{\mathcal{D}} \chi_{\phi}\left(\phi\right) \mathrm{d}\mathcal{D} - \underbrace{\left(V_{\mathrm{lim}} + \left(V_0 - V_{\mathrm{lim}}\right) \max\left(0, 1 - \frac{i}{n_{\mathrm{vol}}}\right) \right)}_{G_{\mathrm{lim}}}, \tag{14}$$

where V_0 is the volume of the initial design configuration, and $\alpha_1 = 4$ and $\alpha_2 = -0.02$ denote the adjusting parameters [5]. It is noteworthy that the third term on the right-hand side of Eq. (14) serves as an additional component aimed at relaxing the upper limit of the volume constraint to facilitate stable convergence such that when the current iteration number is higher than the relaxed iteration number n_{vol}, the relaxed volume constraint in Eq. (14) returns to the primitive one as in Eq. (4).

Solving Eq. (8) using the above modified AL method and its variations has a noticeable drawback: it does not guarantee the accuracy of the volume constraint in the final optimization configuration. To overcome this limitation, this study adopts the EVCM proposed in [15]. In this approach, the exact value of the Lagrange multiplier λ is obtained by decomposing the original RDE (8) into two initial boundary value problems as follows

$$\left(\mathcal{E}_1\right): \begin{cases} \dfrac{\partial \hat{\phi}}{\partial t} = \zeta d_t \mathfrak{L} + \tau \nabla^2 \hat{\phi}, & \text{in } \mathcal{D} \\ \dfrac{\partial \hat{\phi}}{\partial n} = 0, & \text{on } \partial\mathcal{D} \backslash \partial\mathcal{D}_N \\ \hat{\phi} = 1, & \text{on } \partial\mathcal{D}_N \\ \hat{\phi}\left(t\right) = \phi\left(t\right), & \end{cases} \tag{15}$$

and

$$\left(\mathcal{E}_2\right): \begin{cases} \dfrac{\partial \check{\phi}}{\partial t} = 1 + \tau \nabla^2 \check{\phi}, & \text{in } \mathcal{D} \\ \dfrac{\partial \check{\phi}}{\partial n} = 0, & \text{on } \partial\mathcal{D} \backslash \partial\mathcal{D}_N \\ \check{\phi} = 0, & \text{on } \partial\mathcal{D}_N \\ \check{\phi}\left(t\right) = 0, & \end{cases} \tag{16}$$

where the variable $\hat{\phi}$ in the problem $\left(\mathcal{E}_1\right)$ is the LS field within the interval from t to $t + \Delta t$, wherein Δt is the time increment. Meanwhile, the variable $\check{\phi}$ in the problem $\left(\mathcal{E}_2\right)$ is a

time-independent LS field and incurs only a one-time computational cost in the overall optimization process [15].

As presented in [15], the volume constraint in Eq. (4) can be rewritten as an implicit equation with respect to the Lagrange multiplier λ as follows

$$G(\lambda) = \int_{\mathcal{D}} \chi_{\phi}(\phi(\lambda)) \, \mathrm{d}\mathcal{D} - V_{\mathrm{lim}}. \tag{17}$$

In handling the adjusted volume constraint in Eq. (17), the Newton-Raphson algorithm is applied to determine the value of λ. Detailed information about this algorithm can be referenced in [15]. Notably, to compute the characteristic function $\chi_{\phi}(\phi(\lambda))$, a smoothed Heaviside function is used in the following form

$$H_s(\phi(\lambda)) = \max(\tanh(k\phi(\lambda)), 0), \tag{18}$$

where $k = \left(\sqrt{n} + 1\right)$ at the nth time step, as proposed in [15].

2.5. Finite element approximation

Applying the implicit *Backward Euler* method for time discretization and the standard Galerkin method for spatial discretization [19], the Eqs. (15) and (16) are approximated as follows

$$\int_{\mathcal{D}} \frac{\hat{\phi}^{(t+\Delta t)}}{\Delta t} \cdot \hat{\varphi} \mathrm{d}\mathcal{D} + \tau \int_{\mathcal{D}} \nabla \hat{\phi}^{(t+\Delta t)} \cdot \nabla \hat{\varphi} \mathrm{d}\mathcal{D} = \int_{\mathcal{D}} \left(\zeta d_t \mathfrak{L} + \frac{\phi^{(t)}}{\Delta t} \right) \cdot \hat{\varphi} \mathrm{d}\mathcal{D}, \tag{19}$$

$$\int_{\mathcal{D}} \frac{\check{\phi}^{(t+\Delta t)}}{\Delta t} \cdot \check{\varphi} \mathrm{d}\mathcal{D} + \tau \int_{\mathcal{D}} \nabla \check{\phi}^{(t+\Delta t)} \cdot \nabla \check{\varphi} \mathrm{d}\mathcal{D} = \int_{\mathcal{D}} \check{\varphi} \mathrm{d}\mathcal{D}, \tag{20}$$

where $\hat{\varphi}$ and $\check{\varphi}$ are any test functions. In this study, the criteria for concluding the optimization process are delineated by

$$\left\| \phi^{(t+\Delta t)} - \phi^{(t)} \right\|_{L^{\infty}} < 0.02. \tag{21}$$

In the FEM framework, the discretized systems of RDEs (19) and (20) can be written as follows

$$\left(\frac{1}{\Delta t} \mathbf{M} + \mathbf{D} \right) \hat{\mathbf{\Phi}}^{(t+\Delta t)} = \mathbf{M} \left(\zeta \mathbf{L} + \frac{\mathbf{\Phi}^{(t)}}{\Delta t} \right), \tag{22}$$

$$\left(\frac{1}{\Delta t} \mathbf{M} + \mathbf{D} \right) \check{\mathbf{\Phi}}^{(t+\Delta t)} = \mathbf{N}, \tag{23}$$

where $\mathbf{\Phi} = \bigvee_{e=1}^{n_e} \boldsymbol{\phi}^e$, $\hat{\mathbf{\Phi}} = \bigvee_{e=1}^{n_e} \hat{\boldsymbol{\phi}}^e$, and $\check{\mathbf{\Phi}} = \bigvee_{e=1}^{n_e} \check{\boldsymbol{\phi}}^e$ are the assembly nodal value vectors of LS functions; $\mathbf{N} = \bigvee_{e=1}^{n_e} \boldsymbol{N}^e$ and $\mathbf{L} = \bigvee_{e=1}^{n_e} \boldsymbol{L}^e$ are the assembly nodal value vectors of the

shape function and topological sensitivity, respectively; $\mathbf{M} = \bigvee_{e=1}^{n_e} \boldsymbol{M}^e$ and $\mathbf{D} = \mathbf{D}(\tau) = \bigvee_{e=1}^{n_e} \boldsymbol{D}^e(\tau)$ denote the assembly mass and diffusion matrices, respectively, determined by

$$\boldsymbol{M}^e = \int_{\mathcal{D}^e} (\boldsymbol{N}^e)^T \boldsymbol{N}^e \mathrm{d}\mathcal{D}, \tag{24}$$

$$\boldsymbol{D}^e = \tau \int_{\mathcal{D}^e} (\nabla \boldsymbol{N}^e)^T \nabla \boldsymbol{N}^e \mathrm{d}\mathcal{D}, \tag{25}$$

where n_e is the number of Q4 elements and $\mathcal{D}^e$ is a Q4 element in the uniform regular Q4 mesh of the fixed design domain.

3. NUMERICAL EXAMPLES

This section presents an analysis of two benchmark problems to assess the effectiveness of the proposed method. An isotropic elastic material, characterized by Young's modulus E of 1 and Poisson's ratio ν of 0.3, is employed across all benchmark cases. According to the literature [5], the regularization parameter $\tau = 2 \times 10^{-4}$ is deemed appropriate for achieving a balance between the geometric complexity of the optimized configurations and the value of the objective function, and is thereby adopted in the present study. Based on our experience in numerical analysis and prior study [11], the filter radius $r_{\min}$ in Eq. (11) is selected to be $2.5h$, which is a suitable value for smoothing the topological sensitivity field without changing its value too much. Additionally, during the updating of the LS functions, the value of the time increment Δt is taken equal to 0.1 to secure the numerical stability and convergence for the problems.

3.1. A 2D cantilever beam problem

The first benchmark problem under consideration involves a 2D cantilever beam fixed at one end and subjected to a uniform load applied over a small region at the center of the free end, as shown in Fig. 4(a). The value of the volume limit V_{lim} is set at 50% of the whole design domain. The initial design configuration for most of the analyses of this problem is depicted in Fig. 8(a).

To confirm the effectiveness of the smoothing technique for topological sensitivity to the numerical convergence of the problem, a comparison between results with and without applying this technique in the analyzed results is conducted in Fig. 5. Note that a dynamic body-fitted trimmed Q4 mesh generated by splitting a regular background mesh 80×64 and the exact volume method are used in this comparison. As seen in Fig. 5(a), it is observed that there is a significant fluctuation in the amplitude of the compliance over a range of 20 iterations, beginning from iteration 25 when the smoothing method is not

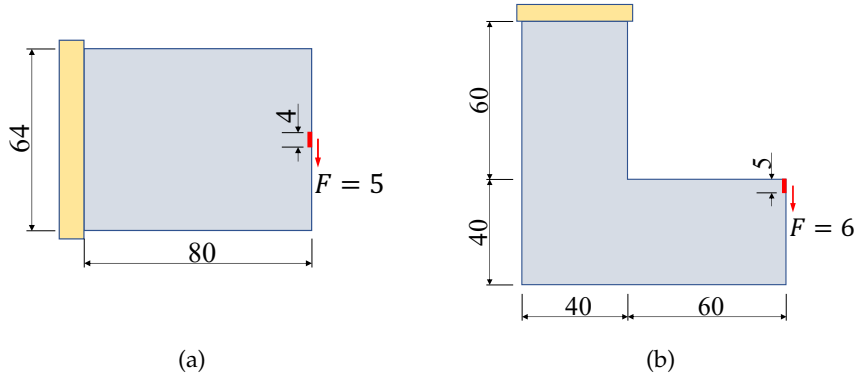

Fig. 4. Two benchmark problems: (a) a 2D cantilever beam, and (b) an L-bracket domain

employed. In contrast, this phenomenon does not occur when the smoothing technique is utilized. Moreover, the convergence time when adopting this technique also decreases considerably, less than half compared to scenarios without it. Additionally, this method can eliminate the minor ripple phenomenon at the interface of the structure, which arises due to the discontinuity of the LS function, as illustrated in Fig. 5(b). These findings verify the superior efficacy of the smoothing method in solving LS-based TO problems, as expected. Therefore, this method will be applied to all subsequent analyses.

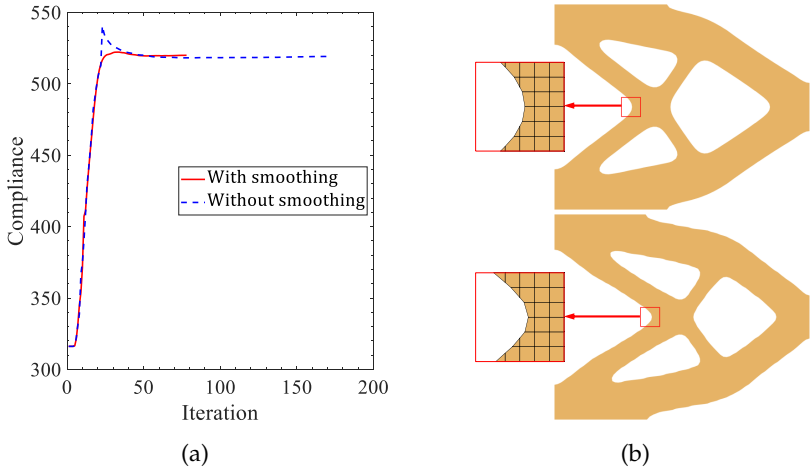

Fig. 5. A comparison of the obtained results with and without applying the smoothing method: (a) compliance history, (b) optimal configurations using the smoothing method (top) and without it (bottom)

Utilizing the same trimmed mesh as specified above, the historical curves of the compliance and volume ratio (V/V_{lim}) for the 2D cantilever beam problem, which are

obtained by using two numerical algorithms in Section 2, are seen in Fig. 6. Overall, a short initial transient, observed as a brief decrease in the volume ratio curve at early iterations, occurs when using the modified AL method. This behavior results from the gradual adjustment of the Lagrange multiplier λ and the concurrent evolution of the smoothed Heaviside function. As both fields converge, the volume ratio rapidly stabilizes at the target value. This transient is purely numerical and does not affect the final topology. Additionally, the volume ratio of the modified AL method at the optimal iteration exhibits a slight deviation (nearly 2%) compared to the value of the volume limit V_{lim}. Although this deviation is relatively minor and generally acceptable, it is important to note that there is no assurance that such a small deviation will remain in other circumstances. In contrast, the volume ratio determined by the exact volume method shows almost no deviation due to the volume constraint at each iterative step being tightly satisfied within the specified error tolerance. Besides, the compliance curve of the exact volume method at the time of convergence is sharply lower than that of the modified AL method. Furthermore, the exact volume method requires less time than the modified AL method to achieve convergence. Through these comparisons, the exact volume method is demonstrated to be capable of enhancing numerical stability and accuracy, as well as significantly improving convergence efficiency in TO problems.

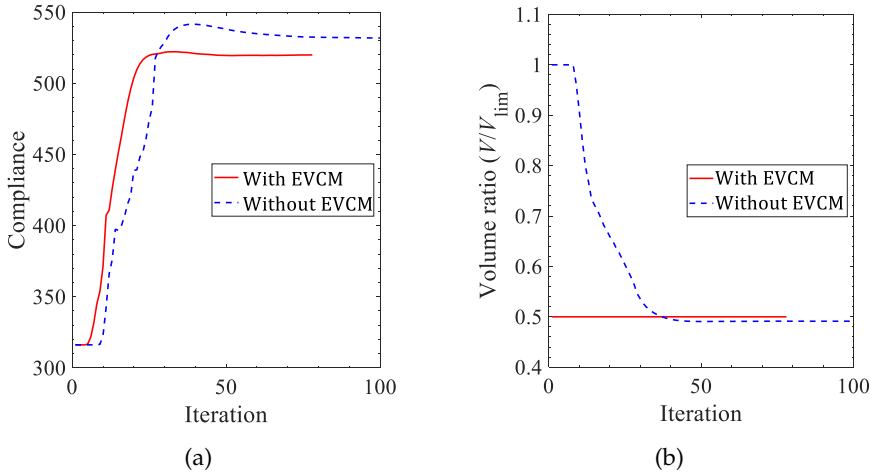

Fig. 6. The historical curves for the 2D cantilever beam problem using modified AL and EVCM methods: (a) compliance and (b) volume ratio

On the other hand, to investigate the influence of using the dynamic body-fitted trimmed Q4 mesh to solve LS-based TO minimum compliance problems, a comparative analysis between this mesh and the regular fixed mesh in the numerical results is featured in detail in Fig. 7. Notably, this analysis uses an 80×64 mesh for the case of the regular fixed mesh (meshing method 1), while the dynamic body-fitted trimmed Q4 (meshing

method 2) is obtained by trimming a regular background mesh having the same mesh size. Both approaches utilize the numerical algorithm of the exact volume method to find the problem solutions. As plotted in Fig. 7(a), it is seen that the compliance curve using meshing method 1 fluctuates considerably during the first 20 iterations, while that using meshing method 2 shows an upward trend until reaching a peak and then falling gradually to convergence. Moreover, the compliance value at the optimal iteration employing meshing method 1 is remarkably higher than that recorded for meshing method 2, while the convergence time of both is not too different. Fig. 7(b) reveals a zig-zag boundary phenomenon of the mechanical structure in the optimal configuration as a result of meshing method 1. In contrast, meshing method 2 yields a crisp and smooth representation of the material boundary. From the results obtained, the dynamic body-fitted mesh evolution method using trimmed Q4 elements proves to be an effective tool for obtaining a clear and explicit representation of the mechanical model while ensuring high accuracy and convergence.

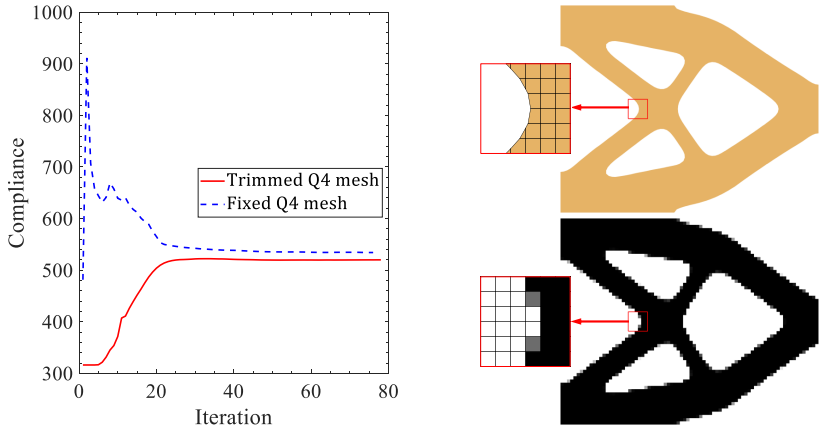

Fig. 7. A comparison of the obtained results for the 2D cantilever beam problem using two meshing methods: (a) compliance history, (b) optimal configurations by using the dynamic body-fitted trimmed Q4 mesh (top) and regular fixed mesh (bottom)

Finally, in order to examine the influence of the initial design configuration on the evolution of the topologies within our proposed method, two distinct cases with different initial design configurations and their corresponding optimal configurations are presented in Fig. 8. It is noteworthy that all the input parameters and the information of dynamic body-fitted trimmed Q4 mesh are the same as in the previous analyses. As shown in Fig. 8, although there is a slight difference in the final shape between the two cases, the optimal configurations in all cases are crisp and smooth. This indicates that the initial design configuration has a minor impact on the resultant optimal configurations.

Furthermore, this figure also exhibits the smooth transition of the topologies throughout the optimization process without any difficulties.

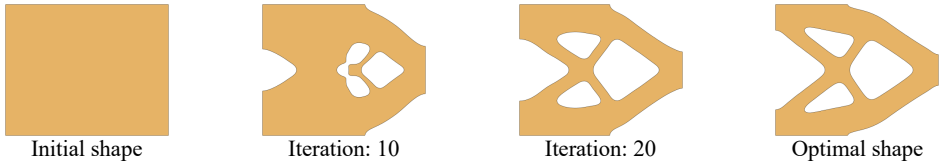

(a) Case 1

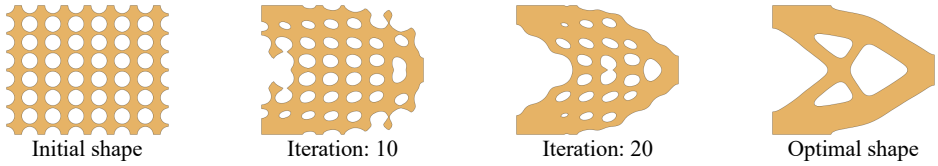

(b) Case 2

Fig. 8. Evolution of the topologies for the 2D cantilever beam problem with different initial design configurations

3.2. An L-bracket domain problem

The second benchmark problem being examined involves an L-bracket domain, fixed at the top edge and subjected to a uniformly distributed load applied over a minor edge

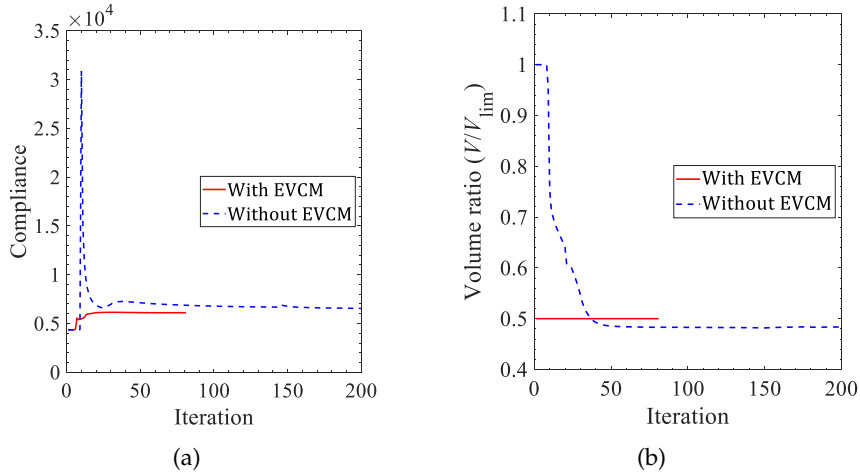

(a) (b)

Fig. 9. The historical curves for the L-bracket domain problem using modified AL and EVCM methods: (a) compliance and (b) volume ratio

at the top right corner of the cantilever part, as depicted in Fig. 4(b). The value of the volume limit V_{lim} is set at 50% of the whole design domain, and the smoothing method for the topological sensitivity is applied for all the cases. In most analyses of this problem, the initial design configuration is established without any holes, as illustrated in Fig. 12(a). Notably, in this example, all the analyses use a uniform 100 $\times$ 40 regular background mesh for both meshing methods.

Fig. 9 illustrates the historical trends of compliance and volume ratio for the L-bracket domain problem, analyzed using two numerical algorithms. It can be seen that the compliance curve derived from the exact volume method exhibits sharply less fluctuation than the modified AL method. Furthermore, the compliance value at the optimal time remains markedly lower with the exact volume method. Besides, the volume ratio for the modified AL method is significantly smaller than the allowable volume ratio at the optimal time. In contrast, the value for the exact volume method always remains accurate and stable during the optimization process. Moreover, less time is spent on convergence in the exact volume method than in the modified AL method.

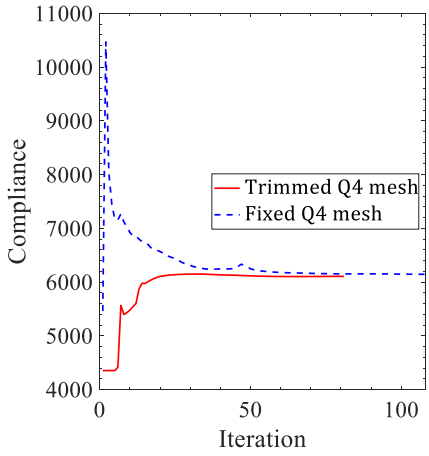

Fig. 10. Compliance history for the L-bracket domain problem using two meshing methods

Figs. 10 and 11 compare the obtained results for the L-bracket domain problem using two distinct meshing methods, as mentioned in Section 4.1. It is evident that the dynamic body-fitted mesh evolution method, using a trimmed Q4 mesh, yields a lower objective function value while taking fewer iterations compared to the conventional fixed mesh approach. Furthermore, it also features a clear and smooth structure boundary without the zig-zag boundary phenomenon arising.

Lastly, the evolution of the topologies of the L-bracket domain at four iterations of the optimization process using two different initial design configurations is viewed in Fig. 12. It is clear that all the topologies have crisp and smooth features, and their evolution can be smoothly changed without any troubles throughout the optimization process by using the proposed approach.

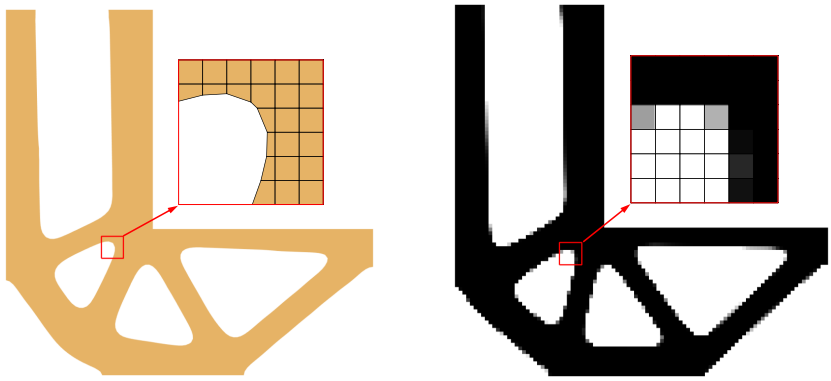

(a) (b)

Fig. 11. Optimal configurations : (a) using the dynamic body-fitted trimmed Q4 mesh and (b) using regular fixed mesh

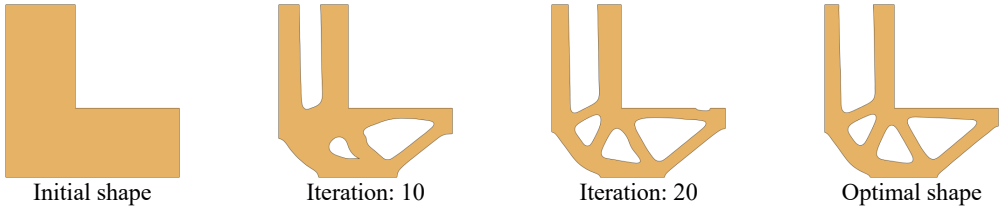

(a) Case 1

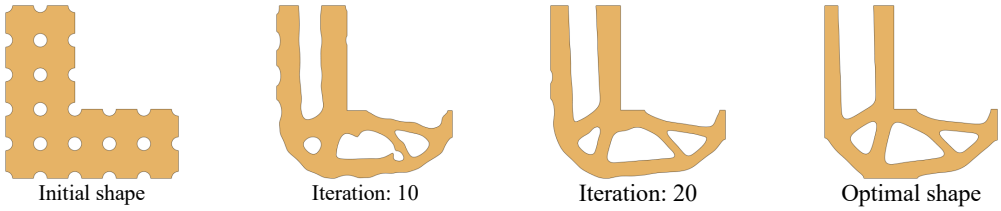

(b) Case 2

Fig. 12. Evolution of the topologies for the L-bracket domain problem with different initial design configurations

4. CONCLUDING REMARKS

This study integrates RDEs with a dynamic body-fitted trimmed Q4 mesh technique to solve LS-based topology optimization problems for compliance minimization. The evolution of the zero-isoline of the LS function is driven by a topological sensitivity field on a regular Q4 mesh and enhanced by a radial smoothing filter to suppress ripple effects

and improve computational efficiency. The dynamic trimmed mesh is generated using the marching square algorithm, while the EVCM accurately computes the Lagrange multiplier for solving the RDE. The results confirm that the smoothing filter enhances numerical stability, the EVCM ensures precise volume control, and the trimmed mesh representation yields smooth and well-defined boundaries. Although the method exhibits high accuracy and robustness, its geometric resolution still depends on the background mesh density, and the current implementation is limited to 2D. Extending the approach to 3D using the marching cube algorithm and trimmed hexahedral meshes is conceptually straightforward but presents additional challenges, such as the complex generation and integration of trimmed elements and the higher computational cost. Despite these limitations, the framework remains promising for large-scale, multi-material, and multi-physics topology optimization problems.

DECLARATION OF COMPETING INTEREST

The authors declare that they have no known competing financial interests or personal relationships that could have appeared to influence the work reported in this paper.

ACKNOWLEDGMENT

This research is funded by Vietnam National Foundation for Science and Technology Development (NAFOSTED) under Grant number 107.02-2023.29.

REFERENCES

[1] Z. Zhuang, F. Xu, J. Ye, W. Tong, Z. Chen, and Y. Weng. A 262-line Matlab code for the level set topology optimization based on the estimated gradient field in the body-fitted mesh. *Structural and Multidisciplinary Optimization*, **67**, (2024). https://doi.org/10.1007/s00158-024-03891-y.

[2] P. Wei, Z. Li, X. Li, and M. Y. Wang. An 88-line MATLAB code for the parameterized level set method based topology optimization using radial basis functions. *Structural and Multidisciplinary Optimization*, **58**, (2018), pp. 831–849. https://doi.org/10.1007/s00158-018-1904-8.

[3] M. Cui, M. Pan, J. Wang, and P. Li. A parameterized level set method for structural topology optimization based on reaction diffusion equation and fuzzy PID control algorithm. *Electronic Research Archive*, **30**, (7), (2022), pp. 2568–2599. https://doi.org/10.3934/era.2022132.

[4] T. Yamada, K. Izui, S. Nishiwaki, and A. Takezawa. A topology optimization method based on the level set method incorporating a fictitious interface energy. *Computer Methods in Applied Mechanics and Engineering*, **199**, (2010), pp. 2876–2891. https://doi.org/10.1016/j.cma.2010.05.013.

[5] M. Otomori, T. Yamada, K. Izui, and S. Nishiwaki. Matlab code for a level set-based topology optimization method using a reaction diffusion equation. *Structural and Multidisciplinary Optimization*, **51**, (2015), pp. 1159–1172. https://doi.org/10.1007/s00158-014-1190-z.

[6] G. Allaire, F. Jouve, and A. M. Toader. Structural optimization using sensitivity analysis and a level-set method. *Journal of Computational Physics*, **194**, (2004), pp. 363–393. https://doi.org/10.1016/j.jcp.2003.09.032.

[7] M. P. Bendsøe and O. Sigmund. *Topology optimization, theory, methods and applications*. Springer Berlin Heidelberg, Berlin, Heidelberg, 2nd edition, (2004). https://doi.org/10.1007/978-3-662-05086-6.

[8] Y. M. Xie and G. P. Steven. *Evolutionary structural optimization*. Springer London, London, New York, (1997). https://doi.org/10.1007/978-1-4471-0985-3.

[9] K. Abe, S. Kazama, and K. Koro. A boundary element approach for topology optimization problem using the level set method. *Communications in Numerical Methods in Engineering*, **23**, (2007), pp. 405–416. https://doi.org/10.1002/cnm.919.

[10] K. E. Jensen. Solving stress and compliance constrained volume minimization using anisotropic mesh adaptation, the method of moving asymptotes and a global p-norm. *Structural and Multidisciplinary Optimization*, **54**, (2016), pp. 831–841. https://doi.org/10.1007/s00158-016-1439-9.

[11] S. H. Nguyen and H. G. Kim. Level set based shape optimization using trimmed hexahedral meshes. *Computer Methods in Applied Mechanics and Engineering*, **345**, (2019), pp. 555–583. https://doi.org/10.1016/j.cma.2018.11.006.

[12] S. H. Nguyen and H.-G. Kim. Stress-constrained shape and topology optimization with the level set method using trimmed hexahedral meshes. *Computer Methods in Applied Mechanics and Engineering*, **366**, (2020). https://doi.org/10.1016/j.cma.2020.113061.

[13] T. Ho-Nguyen-Tan and H.-G. Kim. Level set-based topology optimization for compliance and stress minimization of shell structures using trimmed quadrilateral shell meshes. *Computers & Structures*, **259**, (2022). https://doi.org/10.1016/j.compstruc.2021.106695.

[14] J. J. Laguardia, E. Cueto, and M. Doblaré. A natural neighbour Galerkin method with quadtree structure. *International Journal for Numerical Methods in Engineering*, **63**, (6), (2005), pp. 789–812. https://doi.org/10.1002/nme.1297.

[15] Y. Cui, T. Takahashi, and T. Matsumoto. An exact volume constraint method for topology optimization via reaction–diffusion equation. *Computers & Structures*, **280**, (2023). https://doi.org/10.1016/j.compstruc.2023.106986.

[16] E. L. Wachspress. *A rational finite element basis*. Academic Press, New York, (1975).

[17] D. Adalsteinsson and J. A. Sethian. The fast construction of extension velocities in level set methods. *Journal of Computational Physics*, **148**, (1999), pp. 2–22. https://doi.org/10.1006/jcph.1998.6090.

[18] D. Peng, B. Merriman, S. Osher, H. Zhao, and M. Kang. A PDE-based fast local level set method. *Journal of Computational Physics*, **155**, (1999), pp. 410–438. https://doi.org/10.1006/jcph.1999.6345.

[19] J. Donea and A. Huerta. *Finite element methods for flow problems*. Wiley, Chichester, (2003). https://doi.org/10.1002/0470013826.